Rock Mechanics and Rock Engineering (2023) 56:6631–6645
https://doi.org/10.1007/s00603-023-03413-0

ORIGINAL PAPER

Experimentally Informed Simulation of Creep Behavior in Shale Rocks Induced by Chemo-mechanical Loading

Ravi Prakash[1] · **Sara Abedi**[1,2]

Received: 9 November 2022 / Accepted: 30 May 2023 / Published online: 19 June 2023

Abstract

Creep deformation in shale rocks is an important factor in many applications, such as the sustainability of geostructures, wellbore stability, evaluation of land subsidence, CO_2 storage, toxic waste containment, and hydraulic fracturing. One mechanism leading to this time-dependent deformation under a constant load is the dissolution/formation processes accompanied by chemo-mechanical interactions with a reactive environment. When dissolution/formation processes occur within the material phases, the distribution of stress and strain within the material microstructure changes. In the case of the dissolution process, the stress carried by the dissolving phase is distributed into neighboring voxels, which leads to further deformation of the material. The aim of this study was to explore the relationship between the microstructural evolution and time-dependent creep behavior of rocks subjected to chemo-mechanical loading. This work uses the experimentally characterized microstructural and mechanical evolution of a shale rock induced by interactions with a reactive brine (CO_2-rich brine) and a non-reactive brine (N_2-rich brine) under high-pressure and high-temperature conditions to compute the resulting time-dependent deformation using a time-stepping finite-element-based modeling approach. Sample microstructure snapshots were obtained using segmented micro-CT images of the rock samples before and after the reactions. Coupled nanoindentation/EDS provided spatial alteration of the mechanical properties of individual material phases due to the dissolution and precipitation processes as a result of chemo-mechanical loading of the samples. The time-dependent mechanically informed microstructures were then incorporated into a mechanical model to calculate the creep behavior caused by the dissolution/precipitation processes independent of the inherent viscous properties of the mineral phases. The results indicate the substantial role of the dissolution/precipitation processes on the viscous behavior of rocks subjected to reactive environments.

Highlights

- A computational scheme incorporating experimental data calculated time-dependent creep strain in shale rock due to chemo-mechanical loading.
- A time-dependent microstructural model and time-stepping finite element model were coupled to build the computational framework.
- Micro-CT imaging and coupled nanoidentation/EDS techniques were utilized in the microstructural model to study the evolution of shale rock exposed to CO_2- and N_2-rich brine, at high-pressure and high-temperature conditions.
- Creep deformation distribution varied based on the extent and spatial variability of the reaction, with different behavior observed under CO_2 and N_2 conditions.
- The results highlight the important role of the interplay between the dissolution and precipitation processes on the VE/VP behavior of rocks in reactive environments.

✉ Sara Abedi
sara.abedi@tamu.edu

[1] Department of Civil Engineering, Texas A&M University, College Station, TX 77843, USA

[2] Department of Petroleum Engineering, Texas A&M University, College Station, TX 77843, USA

Keywords Shale rocks · Chemo-mechanical loading · Rock–fluid interaction · Creep deformation · Microstructural evolution

1 Introduction

Shale rocks exhibit significant creep deformation over spatial and temporal scales, which has important implications for various applications, including the sustainability of geostructures, wellbore stability (Horsrud et al. 1994), evaluation of land subsidence (Abel and Lee 1980; Chang and Zoback 2008), toxic waste containment, and hydraulic fracturing (Fjaer et al. 2008; Rybacki et al. 2017). Several experimental and computational studies suggest that the dissolution of load-bearing phases occurring during the evolution of the microstructure plays a major role in causing viscoelastic/viscoplastic (VE/VP) deformation in multiphasic composites, such as geomaterials (Buscarnera and Das 2016; Hu and Hueckel 2007a, b; Hueckel et al. 2016; Karato and Jung 2003; Rutter 1976; Schimmel et al. 2022). This microstructural evolution could be the result of chemical reactions that occur as a result of interactions with a reactive environment, causing stress/strain redistribution (Ghoussoub and Leroy 2001; Karato and Jung 2003; Niemeijer et al. 2002; Rutter 1976, 1983; Shimizu 1995; Weyl 1959).

Various theoretical models and computational algorithms have been developed to study the role of chemical–mechanical couplings on the stress/strain distribution in porous materials. Continuum thermodynamic models have been used extensively to study the long-term mechanical alteration induced by reactive fluid flow in rocks, for instance, by exploring the dominant mechanisms involved in dissolution/precipitation processes or by studying the solid–fluid phase interfacial transformation due to chemical reactions (Buscarnera and Das 2016; Ghoussoub and Leroy 2001; Heidug and Leroy 1994; Lehner 1990; Tengattini et al. 2014). Models developed within the context of poromechanics have been used to study the chemo-mechanics of porous materials, resulting in notable progress in resolving the chemo-mechanical properties of cementitious materials, such as chemically induced mechanical damage and early age mechanical growth (Coussy 2004; Ulm and Coussy 1995, 1996; Ulm et al. 1999). Progress has also been made in the coupling of chemical reactions and the mechanical properties of geomaterials based on the adjustment of plasticity theory to chemical loading (Gajo et al. 2002, 2015; Hu and Hueckel 2007a; Hueckel et al. 2016). In this context, chemical variables are embodied in the plastic hardening rules such that reactions give rise to expansion/contraction of the elastic domain. This approach has been effective in describing different types of mechanisms, including time-dependent deformation induced by changes in pore fluid chemistry, coupled damage, and dissolution-induced creep of geomaterials (Castellanza et al. 2008; Nova et al. 2003).

From an experimental standpoint, several studies have been performed on the time-dependent mechanical behavior of rocks owing to chemo-mechanical effects (Baud et al. 2009; Clark and Vanorio 2016; Dautriat et al. 2011; Grgic 2011; Neveux et al. 2014). Static and dynamic mechanical measurements were performed and geomechanical models were proposed (Castellanza and Nova 2004; Ciantia et al. 2015; Fernandez-Merodo et al. 2007; Vanorio 2015). Studies have shown that the extent of rock mechanical alteration and the resulting creep deformation due to chemo-mechanical interactions are influenced by the rock composition, fluid chemistry, microstructural and transport properties of the rock, temperature, pressure, reaction time, and specific surface area (Cook et al. 2011; Haldar 2013; Nermoen et al. 2016; Rimstidt et al. 2017). The chemical reactions that occur between rocks and reactive fluids cause microstructural alterations in the rock frame, which lead to short- and long-term debonding processes (Ciantia and Castellanza 2016), alteration of stress patterns, and formation of microcracks (Vanorio 2018). Combined with mechanical loading, these chemo-mechanical interactions can cause additional deformation owing to the pressure solution and compaction (Atkinson 1984; Dewers and Ortoleva 1990; He et al. 2002; Tada and Siever 1989; Wawersik et al. 2001).

These studies have played a vital role in leading investigations and designing a wealth of predictive models (Vanorio 2015). However, some past studies are subject to limitations owing to the macroscopic nature of their investigation. Even when considering pore-scale effects, most conventional models and experimental studies consider the effect of chemo-mechanical loading to be spatially uniform over the bulk scale of the rock. These limitations motivated this study, in which we captured the true microstructural evolution of the rock as a result of interactions with reactive fluids and obtained time-dependent mechanical and deformational behavior at the microscale.

This study made use of experimentally characterized microstructural and mechanical evolution of shale rock induced by interaction with a reactive brine (CO_2-rich brine) and a non-reactive brine (N_2-rich brine) under high-pressure and high-temperature conditions to compute the resulting time-dependent deformation using a time-stepping finite-element-based modeling approach. Digital snapshots generated by micro-computed tomography (micro-CT) imaging before and after the reactions provided a microstructural model of the shale sample. Coupled nanoindentation and energy dispersive X-ray spectroscopy (EDS) revealed the spatial alteration of the mechanical properties of different material phases caused by dissolution and precipitation processes due to the

chemo-mechanical loading of the rock samples. The evolution of the VE/VP properties of the samples was then estimated by combining the microstructural evolution with the stress/deformation distribution within the material with respect to time. For this purpose, the kinematic framework developed by Li et al. (2016) and Kannan and Rajagopal (2011) was adopted to link the microstructural evolution to the change in the stress and strain fields, and dissolution/precipitation-induced creep as a result of rock–fluid interaction. By carrying out calculations on samples reacted with reactive and non-reactive brines, the effects of chemical reactions and the resulting microstructural changes on the time-dependent deformation of the studied samples were investigated.

2 Materials and Methods

2.1 Materials

Creep deformation was calculated for Permian shale samples to illustrate the implementation and applicability of the adopted model. Rock–eval pyrolysis of the Permian sample indicated an organic content of 5.15%. The mass percent composition according to X-ray diffraction analysis showed that the major constituents of the sample were quartz (54.59%), illite (23.31%), and oligoclase feldspar (16.61%). The sample also consisted of dolomite (2.54%), pyrite (1.67%), and siderite (1.27%).

2.2 Experimental Procedure

The rock samples were exposed to CO_2-rich (CO_2 condition) and N_2-rich brine (N_2 condition) in a titanium-made Parr batch dissolution reactor. The samples were submerged in 1 molar NaCl synthetic brine at 100 °C and 12.5 MPa for 2 weeks. The N_2 condition represented the control condition without chemical attacks of the acidic brine and was achieved by injecting N_2 into the reactor. Before and after the reaction experiment, high-resolution images of the sample volume with a voxel size of 3 µm were obtained to characterize the microstructural evolution of the rock. Variations in the X-ray attenuation coefficient were used to segment the various constitutive minerals. The Avizo software was used for image processing and segmentation. Image stack preprocessing and background removal were performed using the steps described by Prakash et al. (2021). Moreover, coupled nanoindentation and EDS were performed on cross-sectional samples before and after the reaction to track the evolution of the mechanical properties of individual material phases as a function of depth from the exposed surface (Prakash et al. 2021). Figure 1 shows the results obtained from micro-CT imaging in terms of the volume fraction of different mineral phases as a function of the distance from the exposed surface. Figure 2 shows the variation in the indentation modulus after 14 days of reaction for the clay-rich and quartz-rich phases along the depth of reaction obtained from the coupled nanoindentation and EDS techniques. Each point in Fig. 2 is the average indentation modulus of a particular mineral phase (clay- or quartz-rich

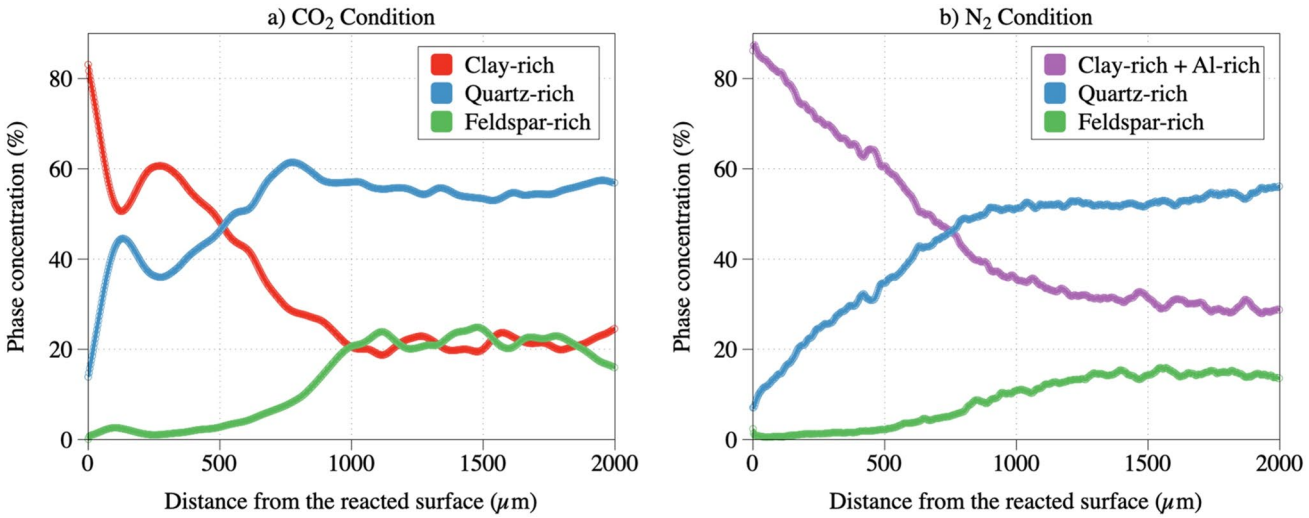

Fig. 1 Variation of volume fraction of different mineral phases as a function of distance from the reacted surface for samples reacted under **a** CO_2 condition and **b** N_2 condition

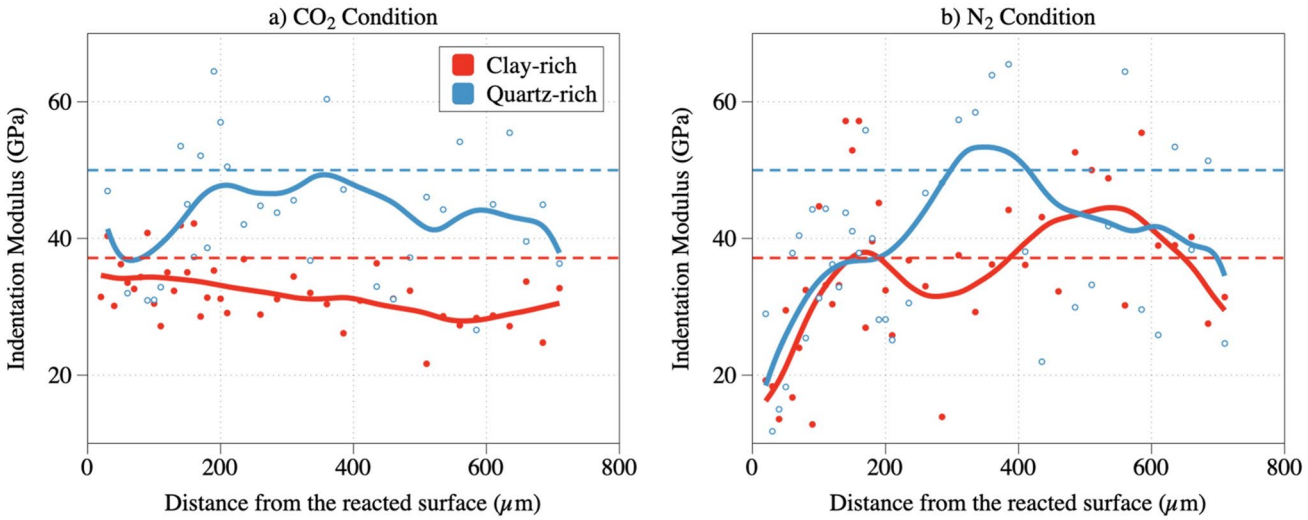

Fig. 2 Variation of indentation modulus as a function of distance from the reacetd surface for clay-rich and quartz-rich phases for samples reacted under **a** CO_2 condition and **b** N_2 condition. Each point shows the average indeintation modulus of clay-rich or quartz-rich phases whitin each column of indentation grid. The solid colored lines represent the overal trend. The dottted lines show the average of indentation moudlus of the unreacted phase

phases) within each column of the nanoindentation grid. The micro-CT results (Fig. 1) indicate the dissolution of feldspar and precipitation of clay close to the reacted surface for samples reacted under CO_2 condition. The quartz particles were also dissolved close to the reacted surface, accompanied by quartz precipitation owing to feldspar transformation in an acidic environment in the sample that reacted under CO_2 condition. Under N_2 condition, Al-rich zones were observed close to the reacted surface. These Al-rich zones were combined with clay-rich zones in the micro-CT image analysis. Such Al-rich zones are observed under neutral pH conditions and result from preferential leaching of Si from feldspar, leaving Al-rich zones in feldspars (Huang and Keller 1970; Huang and Kiang 1972; Kawano and Tomita 1996; Prakash et al. 2021; Reesman and Keller 1965, 1968).

Both the clay-rich and quartz-rich phases are weakened and become more porous by the dissolution of mineral grains for the entire depth of analysis (710 μm) under CO_2 condition. This dissolution of mineral grains is accompanied by the secondary mineral precipitation of clay and quartz closer to the reacted surface, resulting in a higher modulus of these phases in a narrow zone adjacent to the exposed surface. These precipitations result from the dissolution of feldspar and precipitation of kaolinite and phyllosilicate minerals such as smectite, illite (Hangx and Spiers 2009; Lu et al. 2013), and quartz grains as the reaction proceeds (Yuan et al. 2019).

For the sample that reacted under N_2, Fig. 2b shows a high-intensity reaction close to the reacted surface, limited to a depth of approximately 200 μm. This decreased modulus can be attributed to weathering and washing of grains close to the surface, making the sample more porous and softer. After a depth of 200 μm, the indentation moduli of both the quart-rich and clay-rich phases matched those of the unreacted sample. The reader can refer to Prakash et al. (2023) for more details on the experimental procedure.

2.3 Computational Methodology

This study integrated an experimentally informed microstructure model and a time-stepping finite-element mechanical model. The microstructure model produces evolving sample microstructures based on the results of micro-CT analysis combined with coupled nanoindentation and SEM/EDS, which are then used in the model to predict the evolution of the deformation and elastic properties of samples over time. More details regarding the utilized methodology are provided in the following sections.

2.3.1 Microstructure Model

The microstructural evolution from unreacted to reacted samples for both CO_2 and N_2 samples was achieved by (1) updating the mineral composition according to the micro-CT analysis and (2) updating the mechanical properties according to the coupled indentation and SEM/EDS data (Prakash and Abedi 2022). As mentioned in Sect. 2.2, micro-CT imaging was performed on unreacted and reacted samples, and then segmentation analysis was performed on those images. To reduce the computational cost and for simplicity, a 2D microstructure with a size of 2400 μm × 1800 μm (800 × 600 pixels) was selected for FEM analysis. The 2D

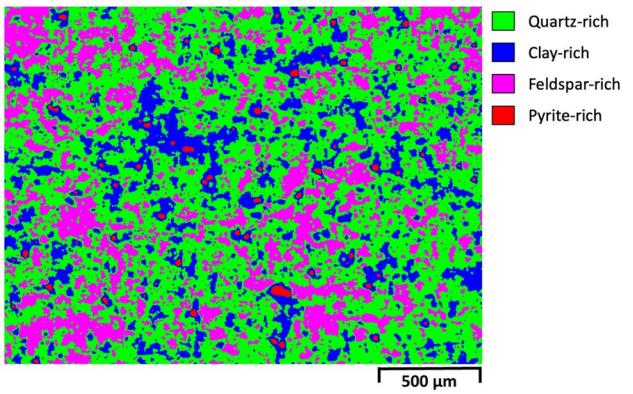

Fig. 3 Microstructure of unreacted Permian shale showing different mineral phases. 2D segmented image is selected such that it is representative of the complete volume

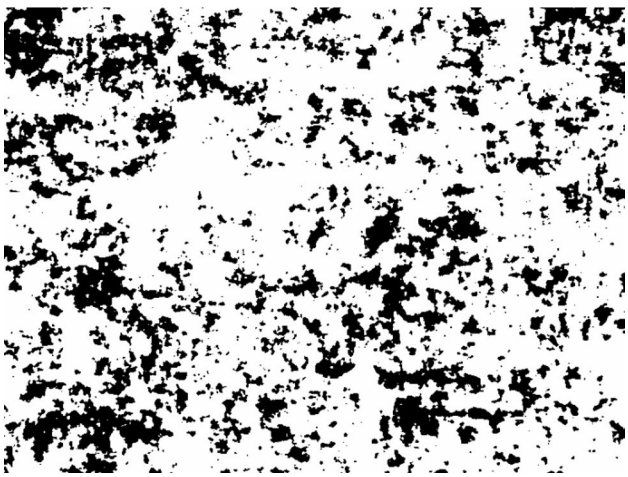

Fig. 4 Binary image of feldspar-rich phases obtained from the unreacted microstructure

segmented image was selected such that it was representative of the complete volume and had the same composition as the complete volume.

The model used in the analysis obtained its geometry directly from the microstructure, and the size of the elements in the finite element method was governed by the size of the voxels in the micro-CT images (3 µm). The geometry was discretized such that each pixel was an element. The term pixel, instead of voxel, is used here because it is a 2D analysis. Each pixel (consisting of a unique phase) was a four-node bilinear square element. It should be noted that increasing image resolution or the number of voxels per simulation box length can enhance the accuracy of model predictions (Haecker et al. 2005). In this study, we employed the smallest element size, which corresponds to a voxel. As noted earlier, the 2D segmented image was selected such that it was representative of the complete volume and shared the same composition. Reducing element size below a voxel would refine the mesh but exponentially increase the number of elements, necessitating the selection of a smaller micro-CT image due to high computational costs. However, as explained in Sect. 2.3.1, we refrain from selecting a smaller image since it would not accurately represent the complete volume of the sample. Figure 3 shows the unreacted microstructure of the sample, which contains various mineral phases. This microstructure was a cropped image from one of the segmented image slices of the unreacted sample.

As mentioned in Sect. 2.2, the variation in the concentration of the various mineral phases in relation to the distance to the exposed surface for the reacted samples was obtained for the entire 3D segmented volume (Fig. 1). To generate the microstructure of the reacted samples, microstructural changes were made to the unreacted microstructure. Using the unreacted microstructure, binary images were extracted for each mineral, with black pixels showing that mineral and white regions showing the rest of the microstructure. Figure 4 shows the binary image for the feldspar-rich phases.

Fig. 5 Binary image of unreacted feldspar-rich phases divided into 12 zones for erosion/dilation operations

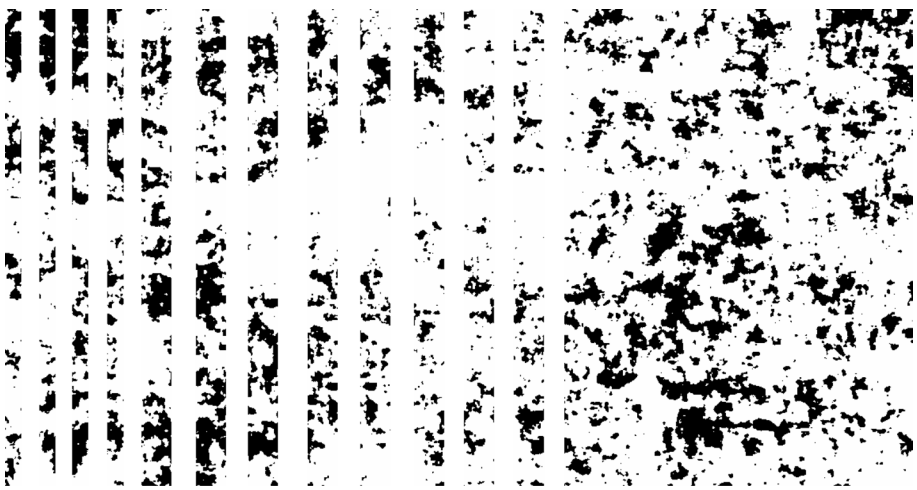

This binary image was used for the erosion operation. Because the volume proportion of feldspar reduces due to dissolution, eroding operations were applied to feldspar-rich phases. The volume fraction of feldspar-rich phases changed with the depth of reaction; hence, different amounts of erosion are required at different locations. To achieve this, the unreacted microstructure was divided into 12 zones (Fig. 5). The size of these zones was decided based on the intensity of the reaction and the extent of microstructural alteration.

Each of the first four zones was 50 × 1800 µm in size, with a longer edge parallel to the exposed surface. The next seven zones were 100 µm × 1800 µm in size. No changes were made to the microstructure of the last (twelfth) zone, representing the unreacted zone. The first four zones were intentionally selected as thinner than the next seven zones because of the sharp variations in the volume fractions closer to the reacted surface, which can be effectively captured using thinner zones. The smallest zone thickness was restricted to 50 µm to maintain continuity in the microstructure, and the maximum thickness was limited to 100 µm to capture the changes in the volume fraction of different material phases (i.e., feldspar-, quartz-, and clay-rich phases) in the microstructure. For each zone of the unreacted microstructure, the average volume percentage of feldspar was calculated, and the erosion operation was applied such that the volume percentage decreased to the average value for the reacted sample in that region. Multiple iterations of the erosion operation were performed to achieve this value. The freeware image analysis software ImageJ was used to perform erosion/dilation operations (Ferreira and Rasb 2012). Once the erosion operation was performed for all the zones individually, all images were stitched together to obtain a full-size image for the feldspar-rich phases.

Eroding operation on the grains was performed for quartz-rich phases close to the reacted surface (dissolution zone), whereas the grains were dilated in certain regions next to the dissolution zone, where the volume fraction of quartz-rich phases slightly increased according to micro-CT results (Fig. 1a). The erosion/dilation procedure and the number/thickness of zones were kept the same as for the feldspar-rich regions to obtain a full-size image for quartz mineral. No changes were made to the pyrite-rich phases; hence, the reacted binary image for pyrite-rich phases was the same as the unreacted binary image of this mineral. Once successfully obtained, all full-size binary images of reacted feldspar-rich, quartz-rich, and pyrite-rich minerals were superimposed together. The remaining regions on the superimposed images were marked as clay. Therefore, the dissolution of feldspar and quartz (cumulative dissolution) resulted in the dilation of the clay regions and increased the volume fraction of clay in the microstructure. Figure 6 shows the resultant microstructure of

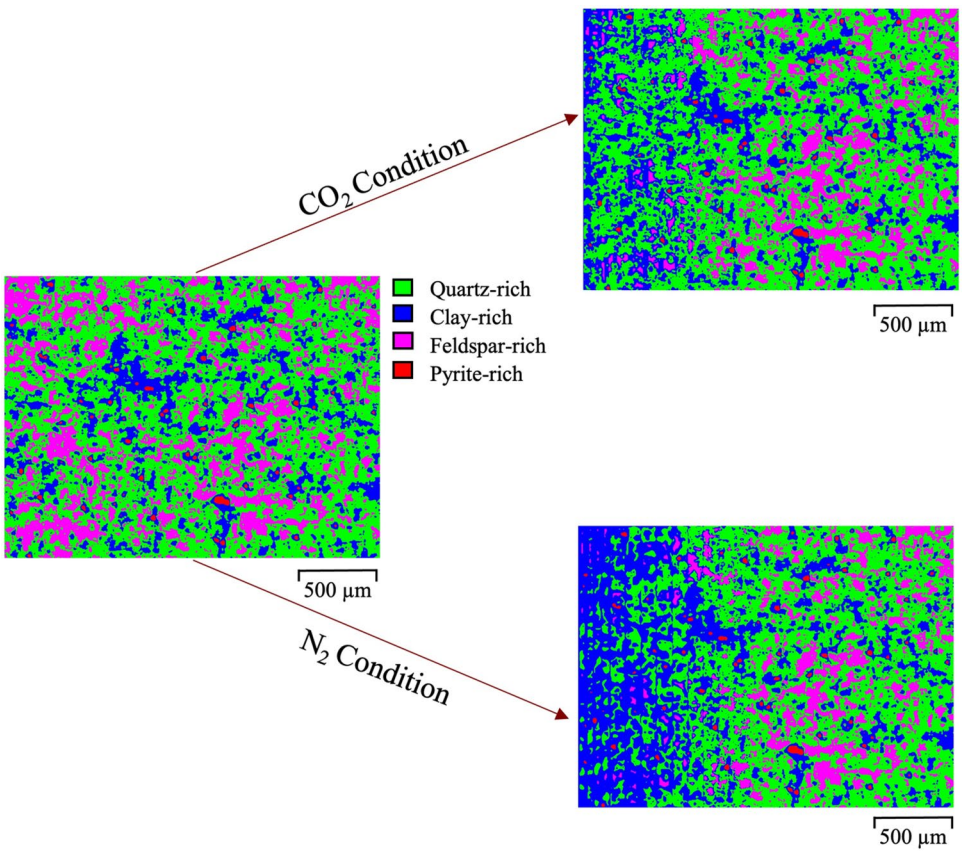

Fig. 6 Microstructure of unreacted Permian shale along with reacted microstructures after 14 days of reaction under CO_2 and N_2 conditions, showing different mineral phases, produced using image analysis. The reacted surface is on the left side of the images. For the sample reacted under N_2 condition, clay-rich zones include Al-rich zones as well

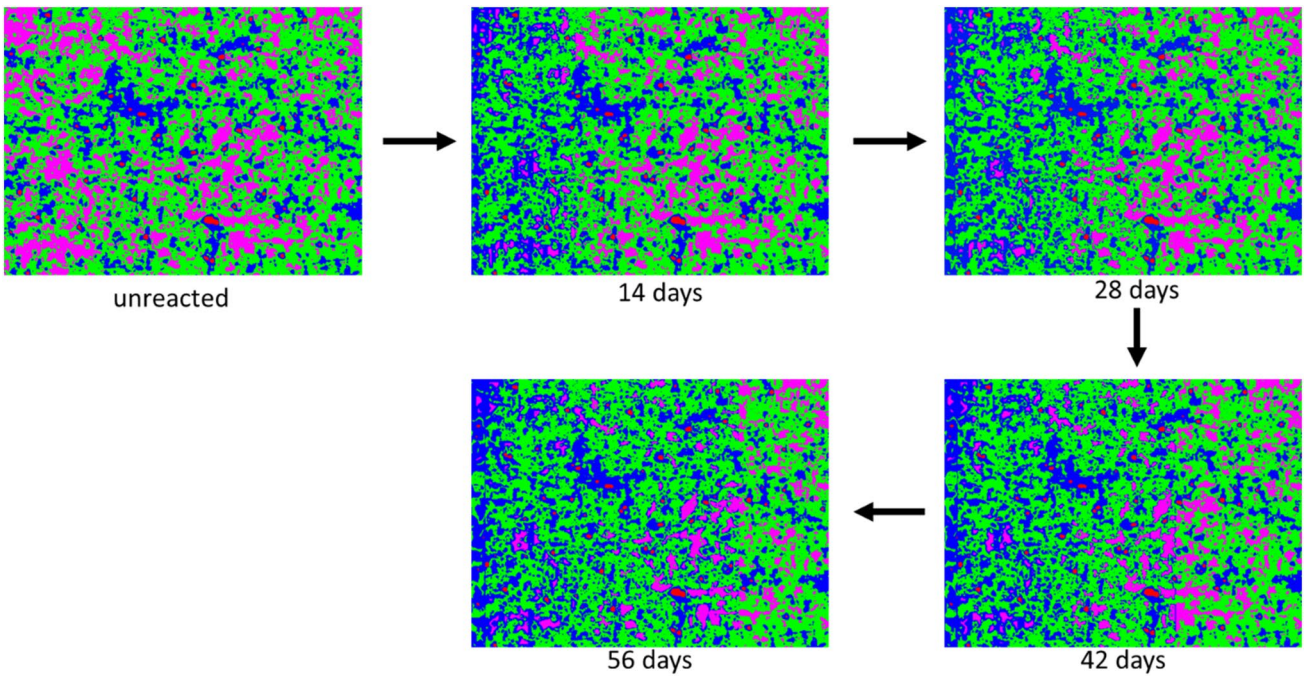

Fig. 7 Microstructure of unreacted Permian shale and after 14, 28, 42, and 56 days of progression of the reaction depth under CO_2 condition, generated using image analysis procedures. The reacted surface is on the left side of the images

the Permian sample after reacting with CO_2 condition and N_2 condition for 14 days.

The effect of the growth of reaction depth over time on creep deformation was also examined for the sample reacted under CO_2 condition. For this purpose, after obtaining the microstructure of the 14-day reaction sample, the microstructure was generated at larger time steps with the assumption that the reaction depth is a function of time, and it follows Fick's law relationship (Fick 1855), that is,

$$D(t_i) = k\sqrt{t_i}, \tag{1}$$

where $D(t_i)$ is the reaction depth at any time t_i, and k is a constant of proportionality. The thickness of each zone was calculated by assuming the above relationship. For example, the zones with a thickness of 50 µm for 14 days increased to a thickness of 70.71 µm after 28 days of reaction. Similarly, the zones with a thickness of 100 µm increased to 141.42 µm. Notably, this part of the study only considers the effect of reaction depth growth; therefore, no changes were made to the volume fraction of minerals within each reaction zone after any time t_i.

Based on these two assumptions, microstructures were generated after 28, 42, and 56 days of the reaction. The steps of the zoning and erosion/dilation methodology remained the same as for the 14-day microstructure. The only change was in the thickness of each zone, depending on the reaction time. Figure 7 shows the microstructure under unreacted condition and after 14, 28, 42, and 56 days of reaction.

2.3.2 Assigning Mechanical Properties

As mentioned previously, coupled nanoindentation and EDS performed on the polished cross-section of the reacted samples was used to obtain the mechanical properties of the individual phases as a function of the reaction depth (Fig. 2). The obtained indentation modulus was assigned to the microstructure. The average indentation moduli of the clay- and quartz-rich phases were calculated for each zone, and the calculated moduli were assigned to the minerals in the specific zones. The indentation modulus of feldspar and pyrite for the reacted microstructure was assumed to be the same as that of the unreacted sample because of the lack of sufficient indentation points on the feldspar- and pyrite-rich phases in the reacted sample. This is a good assumption attributed to the small compositional volumes of these minerals. This assumption simplified the microstructure. This change in the modulus from unreacted to reacted samples was assumed to be constant after 28, 42, and 56 days of reaction. Notably, the thickness of each zone increased at each time step; thus, although the indentation modulus of each depth remained constant, its variation changed with time.

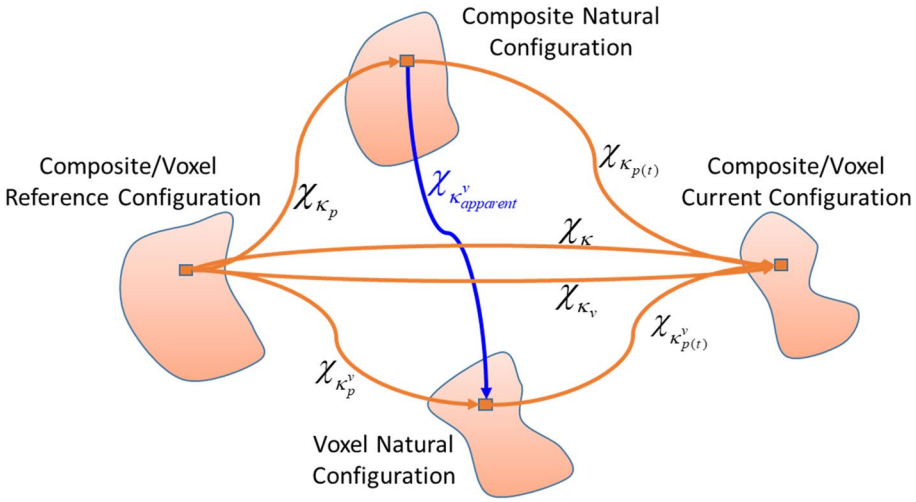

Fig. 8 A schematic view showing the computational framework (adopted form Li et al. (2016))

2.3.3 Conceptualization of the Adopted Kinematic Model

When an elastic material subjected to the dissolution process was exposed to external loading, the entire composite and every voxel/element of the material were deformed from the original configuration to the current configuration. Once the load was removed, the composite did not return to its original configuration, but changed to its natural configuration. The evolution of the natural configuration has been found to cause creep in composite bodies (Kannan and Rajagopal 2011; Li et al. 2016; Rajagopal and Srinivasa 2004).

The complete evolution of the configuration that occurs with the composite also occurs with individual voxels of the composite. The natural configuration of a composite may vary from the natural configuration of the voxel. This difference in motion is referred to as the apparent strain in the composite (Li et al. 2016). Figure 8 provides a graphical depiction of this concept (Li et al. 2016; Rajagopal and Srinivasa 2004). In the context of continuum mechanics, apparent strain is defined as the strain that is present regardless of any external stimuli. Previous studies have demonstrated that the presence of apparent strain is a significant factor contributing to the irreversible dissolution/precipitation-induced creep. To accurately predict the composite material's overall deformation behavior, it is necessary to capture the impact of apparent strain on the inherent stress and strain fields within the composite (Li et al. 2016; Wineman and Rajagopal 2000).

Creep deformation in the multiphasic composite was computed by quantifying the spatially averaged strain field and the spatially averaged stress field within the composite with certain boundary conditions. For a composite body, the spatially averaged stress and strain field can be computed based on the three deformation gradients $\boldsymbol{F}_{k_{p(t)}}$, $\boldsymbol{F}_{k^v_{\text{apparent}}}$, and $\boldsymbol{F}_{K^v_{p(t)}}$ related to the motions $\chi_{k_{p(t)}}$, $\chi_{k^v_{\text{apparent}}}$, and $\chi_{K^v_{p(t)}}$, respectively. By means of these deformation gradients, the Green-Lagrangian strain tensor generated for the motion $\chi_{k_{p(t)}}$ can be expressed as (Li et al. 2016)

$$\boldsymbol{E}_{k_{p(t)}} = \frac{1}{2}\left(\left(\boldsymbol{F}_{k^v_{\text{apparent}}}\boldsymbol{F}_{k^v_{p(t)}}\right)^T\left(\boldsymbol{F}_{k^v_{\text{apparent}}}\boldsymbol{F}_{k^v_{p(t)}}\right) - \boldsymbol{I}\right), \tag{2}$$

where $\boldsymbol{I}$ denotes the identity tensor. Equation (2) can also be written as a function of displacement as:

$$\boldsymbol{E}_{k_{p(t)}} = \left(\text{Grad}_{k^v_p}\boldsymbol{u}^T_{k^v_p} + \boldsymbol{I}\right)\boldsymbol{E}_{k^v_{\text{apparent}}}\left(\text{Grad}_{k^v_p}\boldsymbol{u}_{k^v_p} + \boldsymbol{I}\right) + \boldsymbol{E}_{k^v_{p(t)}}, \tag{3}$$

where $\text{Grad}_{k^v_p}$ represents the gradient operation with respect to the natural voxel configuration. Considering infinitesimal and linearized strains ε, Eq. (3) can be written as

$$\varepsilon_{K_{p(t)}} = \varepsilon_{K^v_{\text{apparent}}} + \varepsilon_{K^v_{p(t)}} \text{ and } \varepsilon = \varepsilon_{\text{apparent}} + \varepsilon_{\text{mechancial}}, \tag{4}$$

where $\varepsilon_{\text{apparent}}$ corresponds to the apparent strain induced by the dissolution-deformation process (i.e., due to chemical reactions), indicating that the $\varepsilon_{apparent}$ encompasses the strain brought about by the changes in rock microstructure linked to chemical reactions. $\varepsilon_{\text{mechancial}}$ is the mechanical strain of the voxel resulting from the stress to which the voxel has been subjected.

2.4 Finite Element Calculation

A finite-element-based homogenization model, elas2d.f, was used to predict the elastic moduli of the composites from 2D reconstructed digital images (Garboczi 1998). This computational scheme uses different microstructural

configurations of the composite at different time steps as inputs and includes the stress distribution effects of the dissolution process. The concept of time steps was included in this computational scheme to account for the historical dependence of the mechanical properties of the material. For a given microstructure at a given time step, the total mechanical energy stored in the entire microstructure should be minimized to achieve mechanical equilibrium. For this analysis, each voxel/element was assumed to behave as a purely linearly elastic material. Then at each time step, the total elastic energy stored in one voxel/element is given by the following equation when the composite is subjected to infinitesimal strain:

$$E_n = \frac{1}{2}\iiint_0^1 \varepsilon_{pq} C_{pqrs} \varepsilon_{rs} \mathrm{d}x\mathrm{d}y\mathrm{d}z, \tag{5}$$

where E_n is the total stored elastic energy, ε_{pq} and C_{pqrs} are the infinitesimal strain tensor and the elastic moduli in full tensorial form, p, q, r, $s = 1$, 2, or 3, respectively, and the integral is over the volume of a single voxel. Equation (5) can be expressed in terms of displacement components according to the following equation:

$$E_n = \frac{1}{2} u_{pq}^T D_{pqrs} u_{rs}, \tag{6}$$

where D_{pqrs} represents the stiffness matrix and u_{pq} represents the q'th component of the displacement at the p'th node. Equation (4) indicates that the strain tensor of any voxel can be approximately represented as the sum of the mechanical and apparent strains, which is applied to the displacement vector at each node as $u_{pq} = U_{pq} + \delta_{pq}^{\text{boundary}} + \delta_{pq}^{\text{apparent}}$. Here, U_{pq} represents the displacement vector set by the neighboring voxels, $\delta_{pq}^{\text{boundary}}$ is a correction vector set by the boundary, and $\delta_{pq}^{\text{apparent}}$ is the correction vector owing to the dissolution-induced apparent strain in the microstructure. Adopting the work of Li et al. (2016, 2017), if we combine the two correction vectors as $\delta_{pq} = \delta_{pq}^{\text{boundary}} + \delta_{pq}^{\text{apparent}}$, and insert it into Eq. (6), we obtain for a given voxel (Garboczi 1998; Garboczi et al. 1999)

$$E_n = \frac{1}{2} u_{pq}^T D_{pqrs} u_{rs} + b_{pq} u_{pq} + C,$$

where

$$b_{rs} = \delta_{pq} D_{pqrs} \text{ and } C = \frac{1}{2} \delta_{pq} D_{pqrs} \delta_{rs}. \tag{7}$$

The exact displacement solution to Eq. (7) can be obtained using Simpson's rule of $\frac{\partial E_n}{\partial u_{pq}} = A_{pqrs} u_{rs} + b_{pq}$, where A_{pqrs} is the Hessian matrix built up from the stiffness matrices of the voxels/elements.

Considering the infinitesimal strain in this work, the stress and strain distributions in the microstructure were obtained by minimizing the total stored mechanical energy using FEM (Garboczi 1998). Owing to the limitations of the computational scheme, only a strain-controlled periodic boundary condition can be applied to the microstructures. In this case, Boltzmann's superposition principle was used to predict the temporal evolution of the creep strain of the microstructure due to the constant external stress (Christensen 2012; Wineman and Rajagopal 2000). First, the composite was exposed to constant periodic volumetric strain to obtain the average hydrostatic stress in the composite. Then this periodic volumetric strain is applied to the composite at different loading ages to calculate the spatially averaged hydrostatic stress as a function of time. As a result of the dissolution and precipitation processes, stress can relax (because of dissolution) or increase (because of precipitation). If both dissolution and precipitation occur, the dominant process determines the stress relaxation or stress increase. If dissolution is the dominant process, additional strain must be applied at each time step to maintain the stress constant. Boltzmann's superposition principle was used to achieve this additional strain according to the following equation (Li et al. 2016)

$$\text{if } i = 1, \varepsilon(t_i) = \frac{-\sigma_0}{3K_{t_i}(t_i)}$$

$$\text{if } i \neq 1, \varepsilon(t_i) = \frac{\sigma_0 - \sum_{k=1}^{i-1}\left[\varepsilon(t_k) K_{t_k}(t_i)\right]}{3K_{t_i}(t_i)}, \tag{8}$$

where σ_0 represents the maintained constant averaged hydrostatic stress, i is the number of time steps, and $i = 1$ corresponds to the initial time step when the external load is applied. The body elastic deformation occurs immediately, $\varepsilon(\mathrm{t_i})$ is the additional linear strain required to attain the constant stress at the boundary, and $K_{t_k}(t_i)$ is the apparent VE/VP bulk modulus of the composite at time t_i when loaded at age t_k. The total strain, which is the sum of the elastic and creep strains as a function of time, can then be obtained by $\varepsilon_{\text{total}}(t_i) = \sum_{k=1}^{i} \varepsilon(t_k)$, where $\varepsilon_{\text{total}}(t_i)$ is the total resultant strain of the composite at any time t_i.

3 Results and discussion

For both CO_2 and N_2 samples, at the first time step ($t_i = 0$), a hydrostatic strain of 130 μm was applied such that the averaged hydrostatic stress was the same as the experimental pressure condition, that is, 12.5 MPa. Multiple iterations, starting from a very small strain value, were performed to determine the correct strain measurement corresponding to a pressure of 12.5 MPa. Figure 9 shows

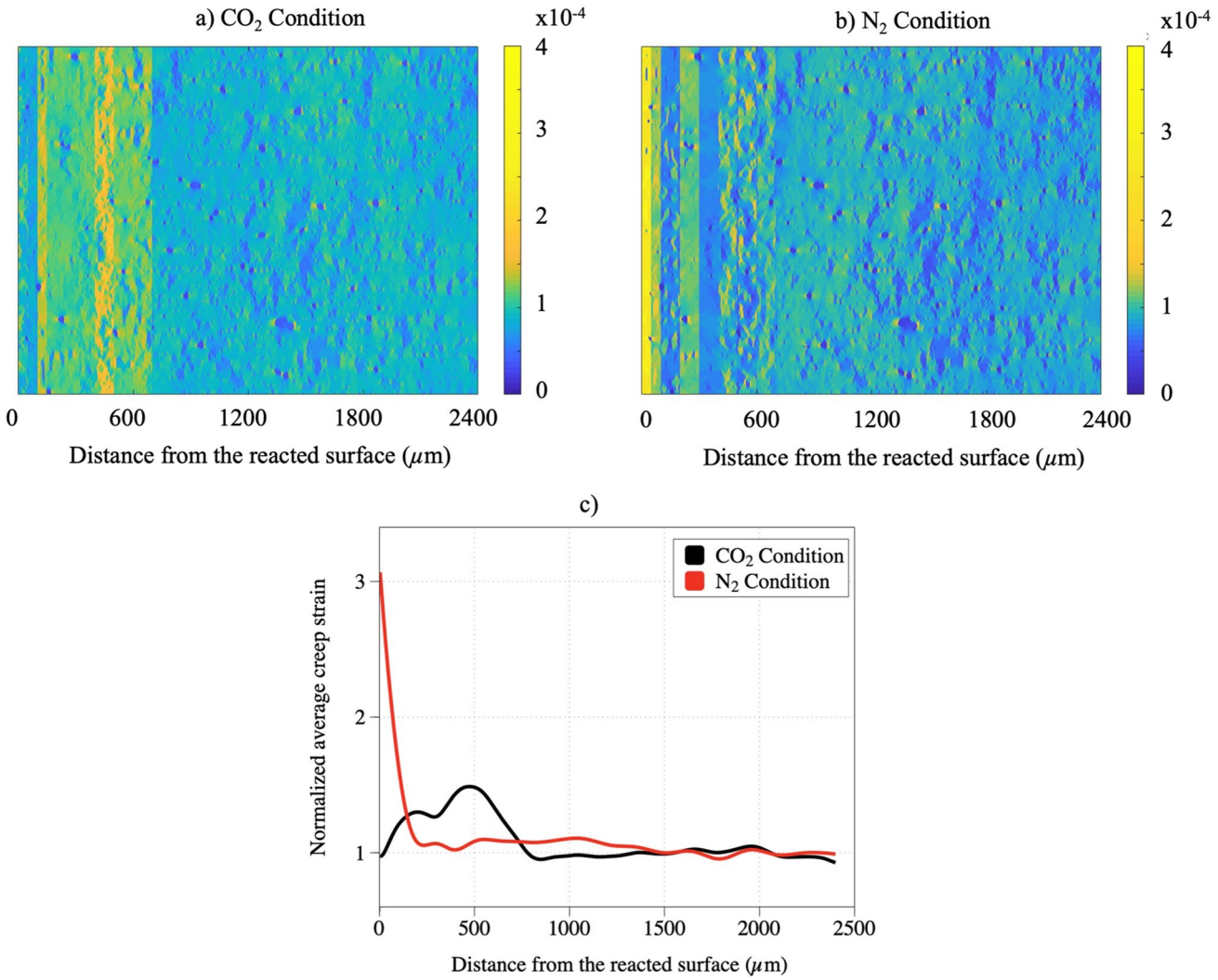

Fig. 9 Contours of creep strain field for **a** CO_2 condition, and **b** N_2 condition after 14 days of reaction. **c** Normalized average creep strain vs. distance from the reacted surface. The reacted surface is on the left side of the images

the creep strain contours and the normalized average creep strain vs. the distance from the reacted surface for the CO_2 and N_2 samples after 14 days of reaction. The average creep strain values were normalized using the creep strain in the unreacted region (Fig. 9c). These results signify the substantial role of the dissolution/precipitation processes on the viscous behavior of rocks subjected to reactive environments.

The spatial distribution of creep deformations under both N_2 and CO_2 conditions is non-uniform and depends on the extent and spatial variability of the reaction. The results showed that the rock that reacted under the N_2 condition experienced a very high creep strain limited to a narrow zone of approximately 200 µm close to the reacted surface. This was due to the softer response of the material as a result of weathering and washing of the grains close to the reacted surface, as well as the precipitation of weak Al-rich phases within that zone. In contrast, for the CO_2 condition, the time-dependent deformation spans an area of approximately 800 µm, corresponding to the severity of the mechanical alteration of different material phases owing to chemical reactions.

Under CO_2 condition, a low creep strain was observed close to the reacted surface until a depth of 100 µm, owing to the precipitation process. The highest amount of creep strain in the CO_2 sample occurred 500–600 µm away from the reacted surface, resulting from the low modulus of clay and quartz at that location. This can be explained by the fact that at the scale of nanoindentation performed in this study, the probed microvolume is composed of a mineral phase intermixed with porosity and organic matter (Abedi et al. 2016a, b; Abedi et al. 2016a, b; Prakash et al. 2021). Therefore, the results obtained by indentation were interdependent on the small porosity between the mineral grains. As discussed

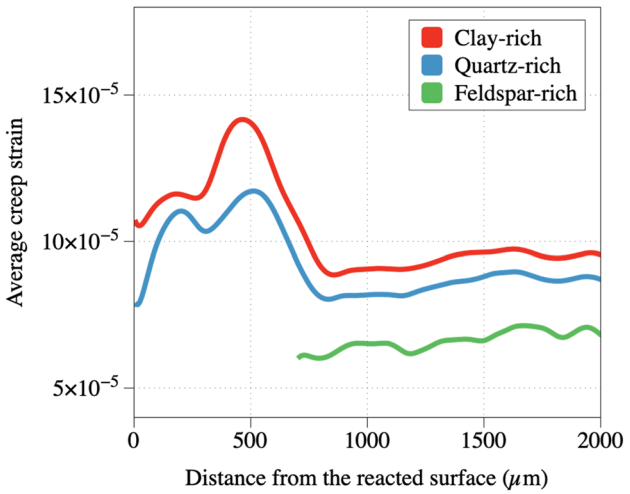

Fig. 10 Average creep strain of clay-, quartz- and feldspar-rich phases vs. distance from the exposed surface for the sample reacted under CO_2 condition for 14 days

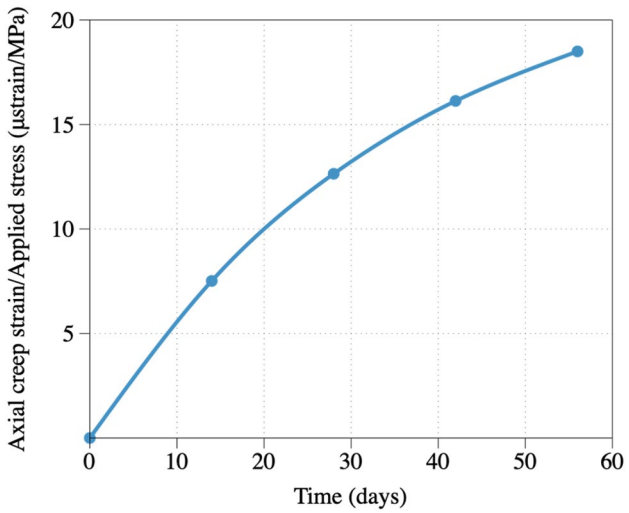

Fig. 11 Axial creep strain of Permian sample with increase in reaction depth over time for the sample reacted under CO_2 condition

in Sect. 2.2 based on the results shown in Fig. 2a, both the clay-rich and quart-rich phases weakened and became more porous compared to the unreacted phases owing to the dissolution of the mineral grains. However, part of the porosity in these phases is filled by precipitation closer to the reacted surface, resulting in increased modulus of these phases in the vicinity of the exposed surface.

Based on the concept of pore-size-controlled solubility (PCS), the level of supersaturation necessary for crystal growth increases with the confinement pressure (Emmanuel and Ague 2009; Varzina et al. 2020). This phenomenon, which is similar to the Ostwald ripening (Nabika et al. 2019; Voorhees 1985) process, in which large crystals grow at the cost of smaller crystals with higher solubility, limits the precipitation of secondary minerals in the nano-porosity between mineral grains. Based on the results presented in Fig. 9, the effect of precipitation on the small pores between grains diminishes at a distance of 500–600 m away from the reacted surface, which causes a lower modulus of clay and quartz, leading to the elevated creep deformation observed at this point. Therefore, the interplay between dissolution and precipitation dictates the amount of time-dependent deformation of rocks, especially when exposed to harsh environments, such as acidic environment caused by CO_2 and brine under high-pressure and high-temperature conditions. This also indicates that the evolution of the pore-size distribution induced by chemo-mechanical interactions plays a key role in the creep properties of rock materials.

To understand the contribution of individual minerals to the total creep strain, the average creep strain of clay-, quartz-, and feldspar-rich minerals was plotted against the distance from the exposed surface for the CO_2 condition after 14 days of reaction (Fig. 10). Clay-rich phases exhibited the highest creep strain, followed by quartz-rich phases, and the lowest creep strain was observed in feldspar-rich phases. Because of the dissolution of feldspar and precipitation of secondary minerals, clay has a very high volume fraction adjacent to the reacted surface; it has lower stiffness compared to quartz, and its modulus has diminished the most in the reacted region. The combination of these effects results in a higher contribution of clay minerals to creep deformation. This plot highlights the effect of the composition of the shale sample on creep strain. A very high volume fraction of clay minerals can increase creep deformation and have more viscous effects on the rock.

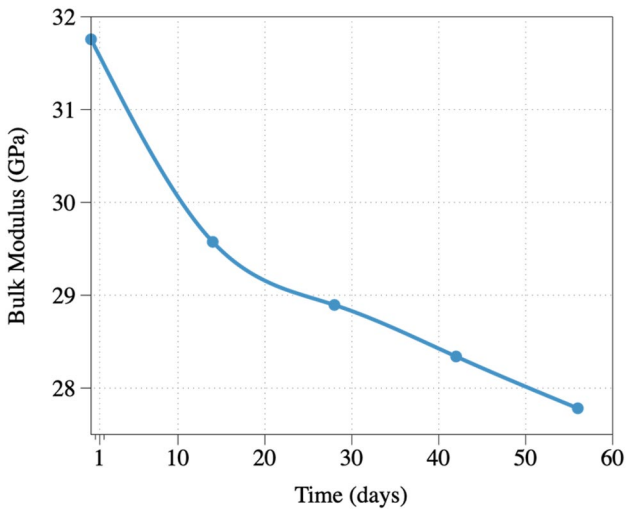

Fig. 12 Viscoelastic bulk modulus of Permian shale with increase in reaction depth over time for the sample reacted under CO_2 condition

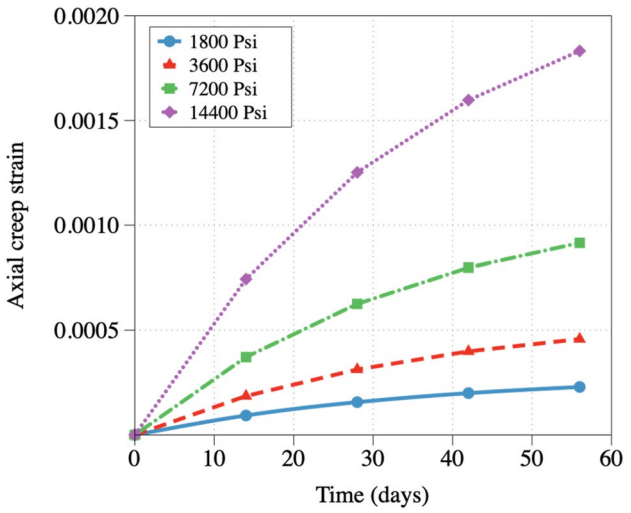

Fig. 13 Change in axial creep strain with increase in the reaction depth over time at different loading for the sample reacted under CO_2 condition

The analysis was further extended to obtain the creep strain under the CO_2 condition when the reaction depth grew over time. This part of the analysis does not account for the mechanical degradation/alteration of the material phases over time and only explores the role of the growth of the reaction depth on creep deformation. Therefore, the results may underestimate creep deformation for a longer reaction duration. Further experimental studies are planned to be conducted for longer durations to capture the effects of both microstructural and mechanical changes on creep deformation as the reaction progresses.

As mentioned in Sect. 2.3.1, for this analysis, a microstructural model was developed with the assumption that the reaction depth is a function of time, and it follows Fick's law (Eq. 1). For the subsequently generated microstructures, the same boundary conditions were applied to the updated microstructure. Stress relaxation was observed at each time step, indicating the dominance of the dissolution reaction. The creep strain at all time steps was calculated using Boltzmann's equation (Eq. 8). Figure 11 shows the predicted creep of Permian shale, excluding the instantaneous elastic deformation due to loading. Each creep strain value in the corresponding figure represents the total creep at the end of the loading period. As depicted in Fig. 11, the shale sample continues to deform under constant loading due to the progression of the reaction depth, even without considering further mechanical alteration of the material phases as the reaction evolves. Figure 12 shows the decrease in the VE/VP bulk modulus of Permian shale with increasing reaction depth.

Batch-type experiments performed in the laboratory have limitations on the pressure inside the reaction chamber; hence, in this study, the experiments were performed at a pressure of 1800 psi. However, shale rocks can experience very high-pressure values deep inside the rock bed. An FEM analysis was performed to compute the creep strain at higher pressure values. Simulations were performed at 24.8, 49.6, and 99.28 MPa (3600, 7200, and 14,400 Psi). Although both thermodynamics and reaction kinetics are expected to be affected by the state of pressure applied to rocks, for simplification in the analysis, the reactivity and alteration in the mechanical properties of the shale minerals were assumed to be constant with an increase in pressure. At all these pressure values, the creep strain was calculated for all loading ages (14, 28, 42, and 56 days), as it was calculated for the 12.5 MPa condition. The results showed that the creep strain increased with increasing applied pressure (Fig. 13). Further experimental and modeling work is required to quantify the real extent of the reaction over time as a function of pressure to obtain a more realistic picture of the creep strain as the reaction progresses with time.

Notably, the bulk modulus obtained reflects the viscoelastic response of an area with the size of 2400 µm × 1800 µm of a shale rock subjected to hydrostatic loading. This viscoelastic response is dependent on the size of the simulation box. Here, we focused on the region in the vicinity of the reacted surface.

4 Conclusion

A computational scheme integrated with experimentally measured microstructural and mechanical data was adopted to calculate the time-dependent creep strain of shale rock induced by chemo-mechanical loading. A time-dependent microstructural model and time-stepping finite element model were coupled to build the computational framework.

The microstructural model made use of results from micro-CT imaging and coupled nanoindentation/EDS techniques to obtain the evolution of the microstructure of the samples owing to chemo-mechanical loading. The approach was applied to Permian shale samples to forecast viscoelastic behavior when subjected to CO_2- and N_2-rich brine under high-pressure and high-temperature conditions. The results indicated that when it comes to the effect of rock–fluid interaction on the time-dependent mechanical properties of rocks, the effect of dissolution/precipitation processes during the reaction is substantial toward the viscous properties of rocks.

For both the CO_2 and N_2 conditions, the spatial distribution of the creep deformations was not uniform and depended on the extent and spatial variability of the reaction. The sample that reacted under N_2 condition showed a very high creep strain limited to a narrow zone (i.e., 200 µm) close to the reacted surface. This was due to weathering and

washing of the grains close to the reacted surface, as well as the precipitation of weak Al-rich phases within that zone.

In contrast, for the sample reaction under CO_2 conditions, the time-dependent deformation caused by the dissolution/precipitation processes extended to an area of approximately 800 μm, which corresponds to the severity of the mechanical alteration of different material phases. For this sample, reduced creep deformation was observed near the reacted surface to a depth of 100 μm owing to the precipitation process. The creep deformation reached a maximum 500–600 μm away from the reacted surface, where the effect of precipitation on the small pores between mineral grains diminished. This observation highlights the determining role of the interplay between the dissolution and precipitation processes and the resulting pore size distribution on the VE/VP behavior of rocks when exposed to reactive environments.

The creep strain rate was obtained for different mineral phase components in different reaction zones. The clay-rich phases exhibited the highest creep strain owing to the very high volume fraction of clay close to the reacted surface and its lower stiffness compared to quartz. Further extension of the analysis to consider the growth of the reaction depth over time for CO_2 exposed sample showed a continuous reduction in the VE/VP bulk modulus of the microstructure with time.

Acknowledgements Acknowledgment is made to the National Science Foundation (Grant CMMI-2045242) and to the donors of the American Chemical Society Petroleum Research Fund (PRF 60545-ND9) for supporting this work.

Data availability The data that support the findings of this study are available from the corresponding author, Sara Abedi, upon reasonable request.

Declarations

Conflict of interest The authors declare that there is no conflict of interest associated with this publication.

References

Abedi S, Slim M, Hofmann R, Bryndzia T, Ulm F-J (2016a) Nano-chemo-mechanical signature of organic-rich shales: a coupled indentation–EDX analysis. Acta Geotech 11(3):559–572

Abedi S, Slim M, Ulm F-J (2016b) Nanomechanics of organic-rich shales: the role of thermal maturity and organic matter content on texture. Acta Geotech 11(4):775–787

Abel JF, Lee FT (1980) Subsidence potential in shale and crystalline rocks. US Geological Survey, Reston, pp 2331–1258

Atkinson BK (1984) Subcritical crack growth in geological materials. J Geophys Res Solid Earth 89(B6):4077–4114

Baud P, Vinciguerra S, David C, Cavallo A, Walker E, Reuschlé T (2009) Compaction and failure in high porosity carbonates: mechanical data and microstructural observations. Pure Appl Geophys 166(5–7):869–898

Buscarnera G, Das A (2016) Chemo-mechanics of cemented granular solids subjected to precipitation and dissolution of mineral species. Int J Numer Anal Meth Geomech 40(9):1295–1320

Castellanza R, Nova R (2004) Oedometric tests on artificially weathered carbonatic soft rocks. J Geotech Geoenviron Eng 130(7):728–739

Castellanza R, Gerolymatou E, Nova R (2008) An attempt to predict the failure time of abandoned mine pillars. Rock Mech Rock Eng 41(3):377–401

Chang C, Zoback M (2008) Creep in unconsolidated shale and its implication on rock physical properties. The 42nd US Rock Mechanics Symposium (USRMS)

Christensen R (2012) Theory of viscoelasticity: an introduction. Elsevier, Amsterdam

Ciantia MO, Castellanza R (2016) Modelling weathering effects on the mechanical behaviour of rocks. Eur J Environ Civ Eng 20(9):1054–1082

Ciantia MO, Castellanza R, Crosta GB, Hueckel T (2015) Effects of mineral suspension and dissolution on strength and compressibility of soft carbonate rocks. Eng Geol 184:1–18

Clark AC, Vanorio T (2016) The rock physics and geochemistry of carbonates exposed to reactive brines. J Geophys Res Solid Earth 121(3):1497–1513

Cook JE, Goodwin LB, Boutt DF (2011) Systematic diagenetic changes in the grain-scale morphology and permeability of a quartz-cemented quartz arenite. AAPG Bull 95(6):1067–1088

Coussy O (2004) Poromechanics. Wiley, New York

Dautriat J, Gland N, Dimanov A, Raphanel J (2011) Hydromechanical behavior of heterogeneous carbonate rock under proportional triaxial loadings. J Geophys Res 116(B01205). https://doi.org/10.1029/2009JB000830

Dewers T, Ortoleva P (1990) A coupled reaction/transport/mechanical model for intergranular pressure solution, stylolites, and differential compaction and cementation in clean sandstones. Geochim Cosmochim Acta 54(6):1609–1625

Emmanuel S, Ague JJ (2009) Modeling the impact of nano-pores on mineralization in sedimentary rocks. Water Resourc Res. https://doi.org/10.1029/2008WR007170

Fernandez-Merodo J, Castellanza R, Mabssout M, Pastor M, Nova R, Parma M (2007) Coupling transport of chemical species and damage of bonded geomaterials. Comput Geotech 34(4):200–215

Ferreira T, Rasb W (2012) ImageJ user guide: IJ 1.46 r

Fick A (1855) Ueber Diffusion (On Diffusion). Annalen der Physik und Chemie von J. C. Pogendorff 94:59–86

Fjaer E, Holt R, Horsrud P, Raaen A, Risnes R (2008) Petroleum related rock mechanics, 2nd edn. Elsevier BV, Radarweg, p 29 (**1000**)

Gajo A, Loret B, Hueckel T (2002) Electro-chemo-mechanical couplings in saturated porous media: elastic–plastic behaviour of heteroionic expansive clays. Int J Solids Struct 39(16):4327–4362

Gajo A, Cecinato F, Hueckel T (2015) A micro-scale inspired chemo-mechanical model of bonded geomaterials. Int J Rock Mech Min Sci 80:425–438

Garboczi EJ, Bentz DP, Martys NS (1999) 1. Digital images and computer modeling. Experimental methods in the physical sciences, vol 35. Elsevier, Amsterdam, pp 1–41

Garboczi EJ (1998) Finite element and finite difference programs for computing the linear electric and elastic properties of digital images of random materials

Ghoussoub J, Leroy YM (2001) Solid–fluid phase transformation within grain boundaries during compaction by pressure solution. J Mech Phys Solids 49(10):2385–2430

Grgic D (2011) Influence of CO2 on the long-term chemomechanical behavior of an oolitic limestone. J Geophys Res Solid Earth 116(B7)

Haecker C-J, Garboczi E, Bullard J, Bohn R, Sun Z, Shah SP, Voigt T (2005) Modeling the linear elastic properties of Portland cement paste. Cem Concr Res 35(10):1948–1960

Haldar SK (2013) Introduction to mineralogy and petrology. Elsevier, Amsterdam

Hangx SJ, Spiers CJ (2009) Reaction of plagioclase feldspars with CO2 under hydrothermal conditions. Chem Geol 265(1–2):88–98

He W, Hajash A, Sparks D (2002) A model for porosity evolution during creep compaction of sandstones. Earth Planet Sci Lett 197(3–4):237–244

Heidug WK, Leroy YM (1994) Geometrical evolution of stressed and curved solid-fluid phase boundaries: 1. Transformation kinetics. J Geophys Res Solid Earth 99(B1):505–515

Horsrud P, Holt RM, Sonstebo EF, Svano G, Bostrom B (1994) Time dependent borehole stability: laboratory studies and numerical simulation of different mechanisms in shale. In: Rock Mechanics in Petroleum Engineering, Delft, Netherlands 29–31 August. https://doi.org/10.2118/28060-MS

Hu LB, Hueckel T (2007a) Coupled chemo-mechanics of intergranular contact: toward a three-scale model. Comput Geotech 34(4):306–327

Hu LB, Hueckel T (2007b) Creep of saturated materials as a chemically enhanced rate-dependent damage process. Int J Numer Anal Meth Geomech 31(14):1537–1565

Huang W, Keller W (1970) Dissolution of rock-forming silicate minerals in organic acids: simulated first-stage weathering of fresh mineral surfaces. Am Mineral J Earth Planet Mater 55(11–12):2076–2094

Huang W, Kiang W (1972) Laboratory dissolution of plagioclase feldspars in water and organic acids at room temperature. Am Mineral J Earth Planet Mater 57(11–12):1849–1859

Hueckel T, Hu L, Hu M (2016) Coupled chemo-mechanics: a comprehensive process modeling for Energy Geotechnics. In: Energy geotechnics: proceedings of the 1st international conference on energy geotechnics, ICEGT, Germany

Kannan K, Rajagopal K (2011) A thermodynamical framework for chemically reacting systems. Z Angew Math Phys 62(2):331–363

Karato S-I, Jung H (2003) Effects of pressure on high-temperature dislocation creep in olivine. Philos Mag 83(3):401–414

Kawano M, Tomita K (1996) Amorphous aluminum hydroxide formed at the earliest weathering stages of K-feldspar. Clays Clay Miner 44(5):672–676

Lehner FK (1990) Thermodynamics of rock deformation by pressure solution. Deformation processes in minerals, ceramics and rocks. Springer, New York, pp 296–333

Li X, Rahman S, Grasley ZC (2016) Computationally implemented modeling of creep of composite materials caused by phase dissolution. Comput Mater Sci 125:61–71

Li X, Grasley Z, Garboczi EJ, Bullard JW (2017) Simulation of the influence of intrinsic CSH aging on time-dependent relaxation of hydrating cement paste. Constr Build Mater 157:1024–1031

Lu P, Fu Q, Seyfried WE Jr, Hedges SW, Soong Y, Jones K, Zhu C (2013) Coupled alkali feldspar dissolution and secondary mineral precipitation in batch systems–2: New experiments with supercritical CO2 and implications for carbon sequestration. Appl Geochem 30:75–90

Nabika H, Itatani M, Lagzi I (2019) Pattern formation in precipitation reactions: the Liesegang phenomenon. Langmuir 36(2):481–497

Nermoen A, Korsnes RI, Aursjø O, Madland MV, Kjørslevik TA, Østensen G (2016) How stress and temperature conditions affect rock-fluid chemistry and mechanical deformation. Front Phys 4:2

Neveux L, Grgic D, Carpentier C, Pironon J, Truche L, Girard J (2014) Experimental simulation of chemomechanical processes during deep burial diagenesis of carbonate rocks. J Geophys Res Solid Earth 119(2):984–1007

Niemeijer A, Spiers C, Bos B (2002) Compaction creep of quartz sand at 400–600 C: experimental evidence for dissolution-controlled pressure solution. Earth Planet Sci Lett 195(3–4):261–275

Nova R, Castellanza R, Tamagnini C (2003) A constitutive model for bonded geomaterials subject to mechanical and/or chemical degradation. Int J Numer Anal Meth Geomech 27(9):705–732

Prakash R, Nguene PCK, Benoit D, Henkel K, Abedi S (2021) Assessment of local phase to mechanical response link: application to the chemo-mechanical identification of rock phases subjected to reactive environments. J Nat Gas Sci Eng 89:103857

Prakash R, Abedi S (2022) Computational modeling of creep behavior in shales induced by fluid-rock interaction. In: 56th US rock mechanics/geomechanics symposium

Prakash R, Ahmad S, Abedi S (2023) Chemo-mechanical alteration of Permian shale after exposure to CO2-rich brine at high-temperature and high-pressure conditions (**under review**)

Rajagopal KR, Srinivasa AR (2004) On the thermomechanics of materials that have multiple natural configurations Part I: viscoelasticity and classical plasticity. Zeitschrift Für Angewandte Mathematik Und Physik ZAMP 55:861–893

Reesman A, Keller W (1965) Calculation of apparent standard free energies of formation of six rock-forming silicate minerals from solubility data. Am Mineral J Earth Planet Mater 50(10):1729–1739

Reesman A, Keller W (1968) Aqueous solubility studies of high-alumina and clay minerals. Am Mineral J Earth Planet Mater 53(5–6):929–942

Rimstidt JD, Chermak JA, Schreiber ME (2017) Processes that control mineral and element abundances in shales. Earth Sci Rev 171:383–399

Rutter E (1976) A discussion on natural strain and geological structure-the kinetics of rock deformation by pressure solution. Philos Trans R Soc Lond Ser A Math Phys Sci 283(1312):203–219

Rutter E (1983) Pressure solution in nature, theory and experiment. J Geol Soc 140(5):725–740

Rybacki E, Herrmann J, Wirth R, Dresen G (2017) Creep of Posidonia shale at elevated pressure and temperature. Rock Mech Rock Eng 50(12):3121–3140

Schimmel M, Hangx S, Spiers C (2022) Effect of pore fluid chemistry on uniaxial compaction creep of Bentheim sandstone and implications for reservoir injection operations. Geomech Energy Environ 29:100272

Shimizu I (1995) Kinetics of pressure solution creep in quartz: theoretical considerations. Tectonophysics 245(3–4):121–134

Tada R, Siever R (1989) Pressure solution during diagenesis. Annu Rev Earth Planet Sci 17:89

Tengattini A, Das A, Nguyen GD, Viggiani G, Hall SA, Einav I (2014) A thermomechanical constitutive model for cemented granular materials with quantifiable internal variables. Part I—theory. J Mech Phys Solids 70:281–296

Ulm F-J, Coussy O (1995) Modeling of thermochemomechanical couplings of concrete at early ages. J Eng Mech 121(7):785–794

Ulm F-J, Coussy O (1996) Strength growth as chemo-plastic hardening in early age concrete. J Eng Mech 122(12):1123–1132

Ulm F-J, Torrenti J-M, Adenot F (1999) Chemoporoplasticity of calcium leaching in concrete. J Eng Mech 125(10):1200–1211

Vanorio T (2015) Recent advances in time-lapse, laboratory rock physics for the characterization and monitoring of fluid-rock interactions. Geophysics 80(2):WA49–WA59

Vanorio T (2018) Challenges and recent advances in rock physics. In: International geophysical conference, Beijing, China, 24–27 April 2018

Varzina A, Cizer Ö, Yu L, Liu S, Jacques D, Perko J (2020) A new concept for pore-scale precipitation-dissolution modelling in a lattice Boltzmann framework–application to portlandite carbonation. Appl Geochem 123:104786

Voorhees PW (1985) The theory of Ostwald ripening. J Stat Phys 38:231–252

Wawersik WR, Rudnicki JW, Dove P, Harris J, Logan JM, Pyrak-Nolte L, Orr FM Jr, Ortoleva PJ, Richter F, Warpinski NR (2001) Terrestrial sequestration of CO2: an assessment of research needs. Advances in geophysics, vol 43. Elsevier, Amsterdam, pp 97–IX

Weyl PK (1959) Pressure solution and the force of crystallization: a phenomenological theory. J Geophys Res 64(11):2001–2025

Wineman AS, Rajagopal KR (2000) Mechanical response of polymers: an introduction. Cambridge University Press, Cambridge

Yuan G, Cao Y, Schulz H-M, Hao F, Gluyas J, Liu K, Yang T, Wang Y, Xi K, Li F (2019) A review of feldspar alteration and its geological significance in sedimentary basins: from shallow aquifers to deep hydrocarbon reservoirs. Earth Sci Rev 191:114–140